Available online at www.sciencedirect.com
SCIENCE DIRECT
International Journal of Heat and Fluid Flow 27 (2006) 192–203
International Journal of HEAT AND FLUID FLOW
www.elsevier.com/locate/ijhff

Numerical simulation of a precessing vortex breakdown

P. Jochmann *, A. Sinigersky, M. Hehle, O. Schäfer, R. Koch, H.-J. Bauer

Institut für Thermische Strömungsmaschinen, Universität Karlsruhe (TH), Kaiserstr. 12, 76128 Karlsruhe, Germany

Received 29 November 2004; accepted 6 August 2005
Available online 27 September 2005

Abstract

The objective of this work is to present the results of time-dependent numerical predictions of a turbulent symmetry breaking vortex breakdown in a realistic gas turbine combustor. The unsteady Reynolds-averaged Navier–Stokes (URANS) equations are solved by using the k–ϵ two-equation model as well as by a full second-order closure using the Reynolds stress model of Speziale, Sarkar and Gatski (SSG). The results for a Reynolds number of 5.2×10^4, a swirl number of 0.52 and an expansion ratio of 5 show that the flow is emerging from the swirler as a spiral gyrating around a zone of strong recirculation which is also asymmetric and precessing. These flow structures which are typical for the spiral type (S-type) vortex breakdown have been confirmed by PIV and local LDA measurements in a corresponding experimental setup. Provided that high resolution meshes are employed the calculations with both turbulence models are capable to reproduce the spatial and temporal dynamics of the flow.

Keywords: Vortex breakdown; Spiral type; Helical instability; Precessing vortex core; URANS; LDA; PIV

1. Introduction

Vortex breakdown is a very effective way of establishing a recirculation zone in a swirling flow and thus a premise for aerodynamical flame stabilization in high intensity combustion chambers (Gupta et al., 1984). Despite its importance in engineering applications and more than four decades of investigation, there is still no general accepted theory explaining all aspects of the vortex breakdown phenomenon. Specific features like different flow states and the transition between them as well as theoretical attempts to describe the specific states of flow have been presented in comprehensive reviews (Leibovich, 1978, 1984; Escudier, 1987, 1988; Lucca-Negro and O'Doherty, 2001). However, as Hall (1972) stated in an early review "there does not appear to be any simple set of numbers that would fix the position of breakdown". On the other hand, the different patterns of vortex breakdown could be characterized in terms of integral parameters like Reynolds number Re, swirl number S (or swirl parameter Ω) and the expansion ratio E (Sarpkaya, 1971; Faler and Leibovich, 1977). At higher Reynolds numbers, only the bubble form (B-type) and the spiral form (S-type) vortex breakdown have been observed (Leibovich, 1984). For gas turbine combustor flows with Re higher than 1.8×10^4, Gupta et al. (1984) mention two states, one with a large precessing vortex core (PVC) and the other one with a large PVC which is damped depending on the radial pressure gradient. The flow structures described by Gupta et al. (1984) as PVC resemble the S-type vortex breakdown characteristics which have been observed also by other investigators (Sarpkaya, 1971; Faler and Leibovich, 1977). This breakdown type exhibits an internal stagnation point and a zone of reversed flow which according to Leibovich (1978) are key elements of vortex breakdown. In order to avoid any ambiguity, it seems advisable to use the notation of precessing (or S-type) vortex breakdown to distinguish between a precessing vortex breakdown and a precessing vortex core (PVC) without vortex breakdown which was investigated by Guo et al. (2001).

As pointed out by Durbin (2002) recently, Reynolds averaging of the Navier–Stokes equations (RANS) is not limited to statistical stationary flows nor to unsteady flows with a spectral gap between the mean-flow unsteadiness

* Corresponding author. Tel.: +49 721 608 6473; fax: +49 721 608 8740.
E-mail address: Paul.Jochmann@its.uni-karlsruhe.de (P. Jochmann).

0142-727X/$ - see front matter © 2005 Elsevier Inc. All rights reserved.
doi:10.1016/j.ijheatfluidflow.2005.08.003

and the turbulent fluctuations. This finding was confirmed by the unsteady-RANS (URANS) computations of Iaccarino et al. (2003) for the flow over a surface mounted cube, which showed very good agreement with experiments and large eddy simulations (LES). In the case of recirculating highly turbulent swirl flows, Wegner et al. (2004) compared URANS results with LES and experimental data and could prove good coincidence.

In this paper, we will show that the URANS method is capable to predict a spiral type vortex breakdown with a precession frequency of about 1800 Hz in a high Reynolds number swirling flow which is typical for combustion applications. The predicted instantaneous and averaged flow fields are compared to experimental data. A more detailed investigation of the early vortex breakdown stages in the present case suggests a mode selection scenario like that proposed by Ruith et al. (2003) in their numerical investigations of a laminar, unconfined vortex breakdown.

2. Geometry

In this study we concentrate on the CFD prediction of a realistic gas turbine combustor consisting of the swirler and the axisymmetric combustion chamber (Fig. 1). The computational domain as well as the experimental setup included not only the swirler and the combustion chamber as shown in Fig. 1, but also the plenum upstream of the swirler (cf. Fig. 3). The flow inside the plenum was very homogeneous (which was verified by PIV measurements) and thus allowed good experimental control and consistency between the real flow and the prescribed inlet boundary conditions in the computations. The flow enters the swirler radially, is then guided by slots through the swirler and leaves it almost in tangential direction (Fig. 2). The fluid leaves the combustion chamber through a concentric annular channel. As it can be seen from Fig. 1 the flow is axially accelerated by this constriction at the outlet of the combustion chamber. As Escudier and Keller (1985) have pointed out, this helps to turn the flow from a subcritical state after the vortex breakdown to a supercritical flow at the outlet. By this measure, the sensitivity of the recirculation region to the outlet conditions can be reduced and an adequate location for specifying the outlet boundary condition can be found. In an a posteriori evaluation, we have found in the present case swirl angles ($\phi = \arctan\frac{w}{u}$, where w is the tangential and u, the axial velocity component) at

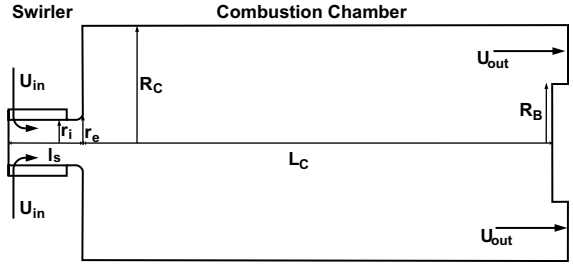

Fig. 1. Geometry of combustor.

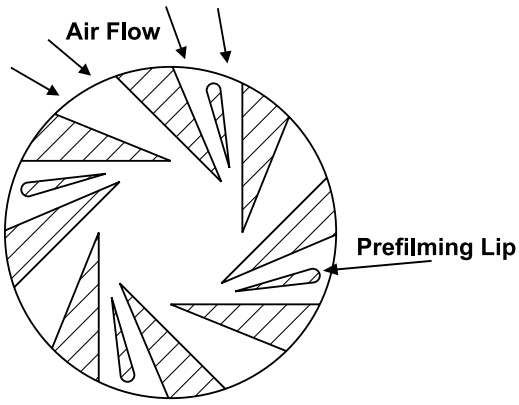

Fig. 2. Cross-section of the swirler.

Table 1
Dimensionless numbers characterizing the flow

Reynolds number	Swirl number	Expansion ratio	Strouhal number
$Re := \frac{\bar{u} \cdot 2r_i}{\nu}$	$S := \frac{\dot{D}_0}{\dot{I}_0 \cdot r_i}$	$E := \frac{R_C}{r_i}$	$Sr := \frac{f \cdot 2r_i}{\bar{u}}$

the outlet of 40° and less, which clearly indicates a supercritical flow in the sense of Squire (1960) and, thus, meets the criterion for a suitable outlet boundary condition, as suggested by Escudier and Keller (1985).

The fluid is air at ambient conditions with no combustion. Because of the low Mach number, the flow can be considered as incompressible. For all calculations presented in this work, the identical global parameters as defined in Table 1 have been used ($Re = 5.2 \times 10^4$, $S = 0.52$ and $E = 5$). In Table 1 $\bar{u}$ denotes the bulk velocity in the nozzle; $\dot{D}_0$, the flux of angular momentum; $\dot{I}_0$, the flux of axial momentum; r_i, the inner radius of the nozzle; and R_C, the combustion chamber radius as indicated in Fig. 1.

3. Computational method

The CFD package *CFX5* was used for solving the Reynolds-averaged Navier–Stokes equations on an unstructured mesh with 2.5×10^6 tetrahedral elements and about

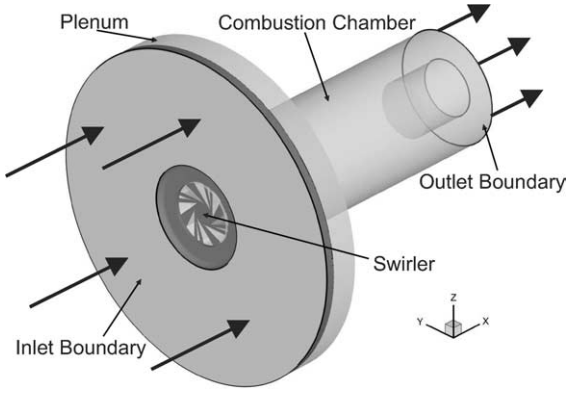

Fig. 3. Computational model including the plenum and the inlet and outlet boundary.

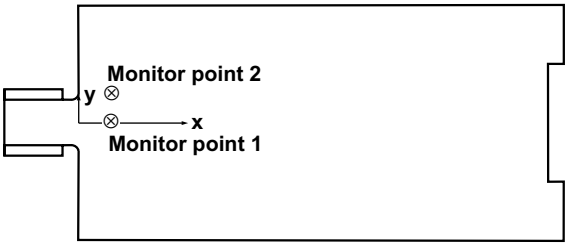

Fig. 4. Location of the monitoring points: point one ($x = 1.5 \cdot r_i$; $y = 0$) and point two ($x = 1.5 \cdot r_i$; $y = 1.2 \cdot r_i$).

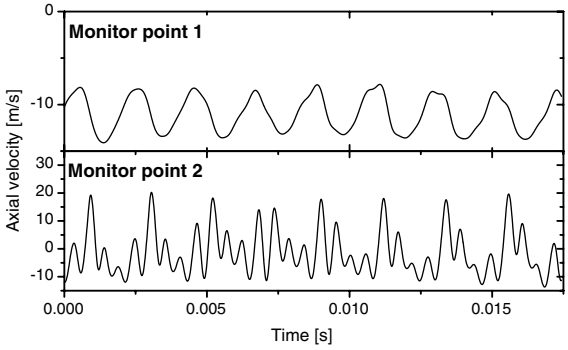

Fig. 5. Time series of the monitoring points obtained from numerical calculation (SSG model).

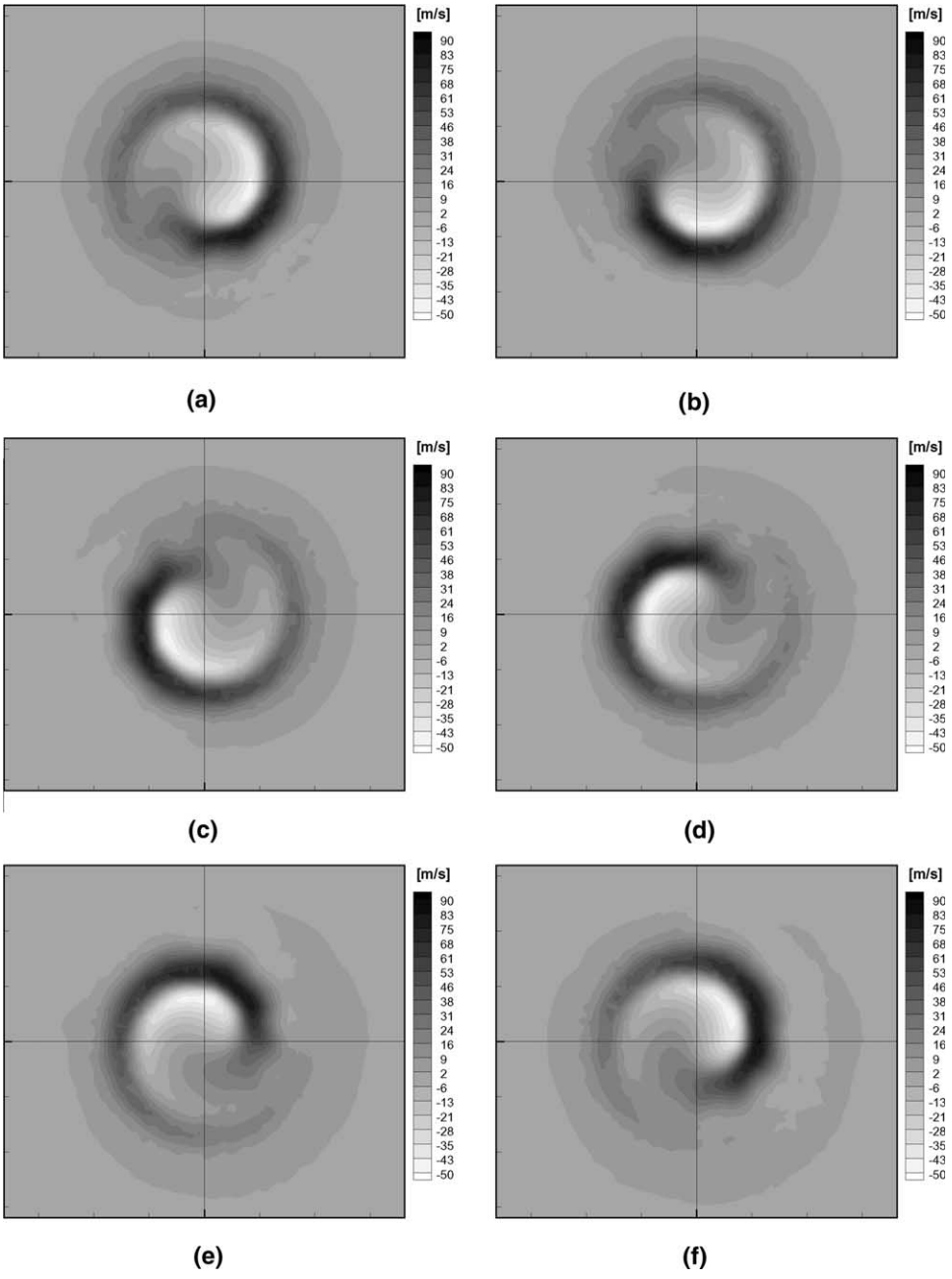

Fig. 6. A period of axial velocity fluctuations in the azimuthal plane 5 mm downstream the swirler exit (SSG model). Phase angle (a) $\varphi = 0$, (b) $\varphi = 2\pi\frac{1}{6}$, (c) $\varphi = 2\pi\frac{2}{6}$, (d) $\varphi = 2\pi\frac{3}{6}$, (e) $\varphi = 2\pi\frac{4}{6}$ and (f) $\varphi = 2\pi\frac{5}{6}$.

0.5×10^6 computational nodes. At the wall, prismatic elements were used for a better boundary layer resolution and pyramidal elements for connecting the tetrahedral with the prismatic elements. A high resolution spatial discretization scheme of second order, which is locally modified for boundedness reasons (Barth and Jespersen, 1989) and a first-order-backward-Euler scheme for temporal discretization were employed. The time step was set to 10^{-5} s which allows the detection of frequencies in the kHz range. In Fig. 3, the complete computational model is presented together with the locations where the inlet and outlet boundary conditions were specified. In order to justify a homogeneous flow at the inlet, the mesh was extended to include the plenum. The inlet velocity was set at the plenum entry uniformly to $u = 0.281$ m/s, which was confirmed by PIV measurements. The turbulence intensity was prescribed to 3% and the turbulent length scale to 5×10^{-3} m. At the outlet boundary condition only the pressure was specified to a value of 1 bar, which corresponds to the ambient pressure of the experiment. Therefore, a very good consistency between the experimental and the numerical setup is ensured regarding the boundary conditions. For the computations presented below steady and symmetric velocity distributions at the inlet were specified. The time-dependent and three-dimensional flow evolved completely naturally. For the analysis of the periodic flow (time series, spectral analysis, averaging, etc.) the time steps for the settling of the flow were neglected. In a second numerical

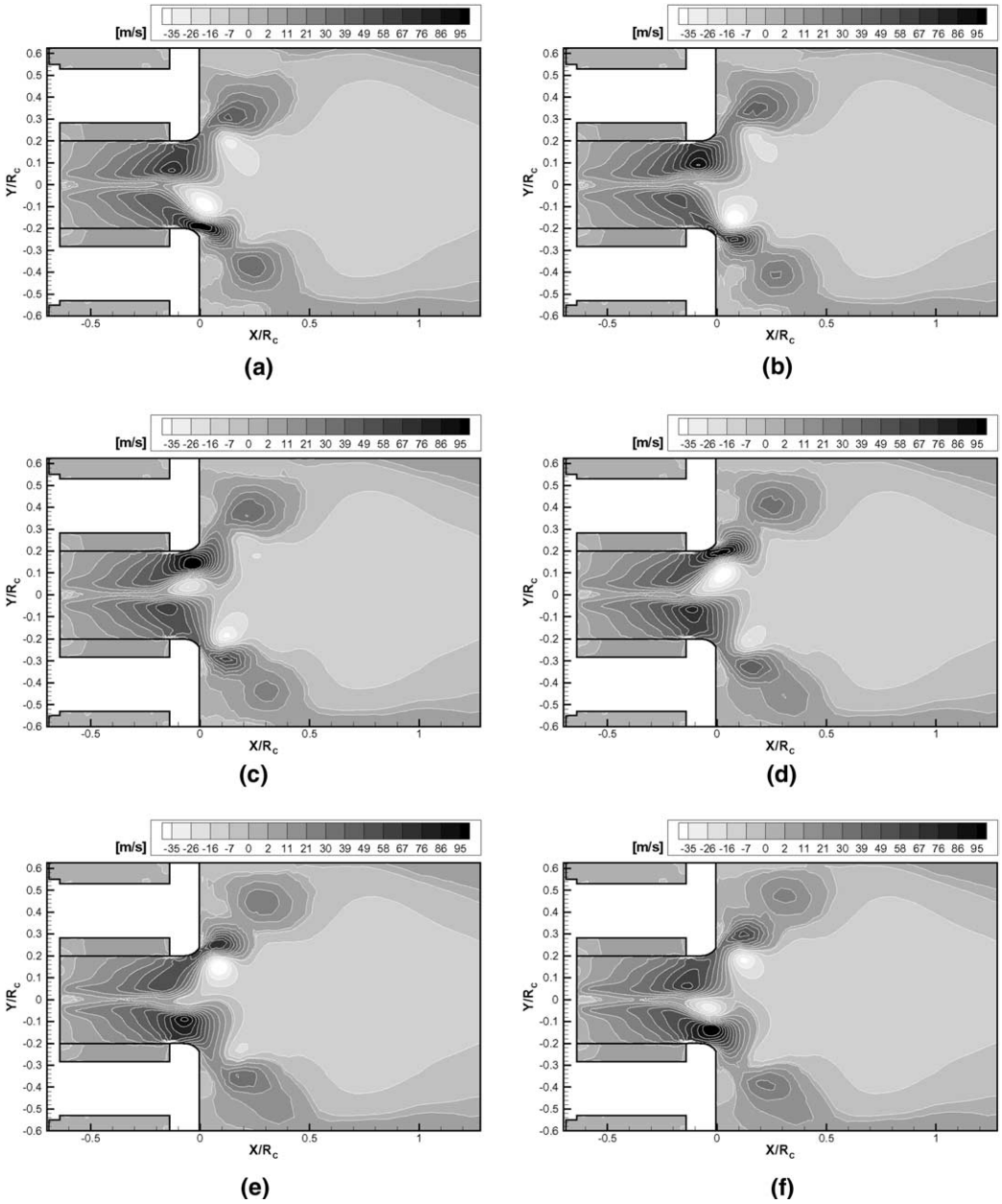

Fig. 7. A period of axial velocity fluctuations in the meridional plane (SSG model). Phase angle (a) $\varphi = 0$, (b) $\varphi = 2\pi\frac{1}{6}$, (c) $\varphi = 2\pi\frac{2}{6}$, (d) $\varphi = 2\pi\frac{3}{6}$, (e) $\varphi = 2\pi\frac{4}{6}$ and (f) $\varphi = 2\pi\frac{5}{6}$.

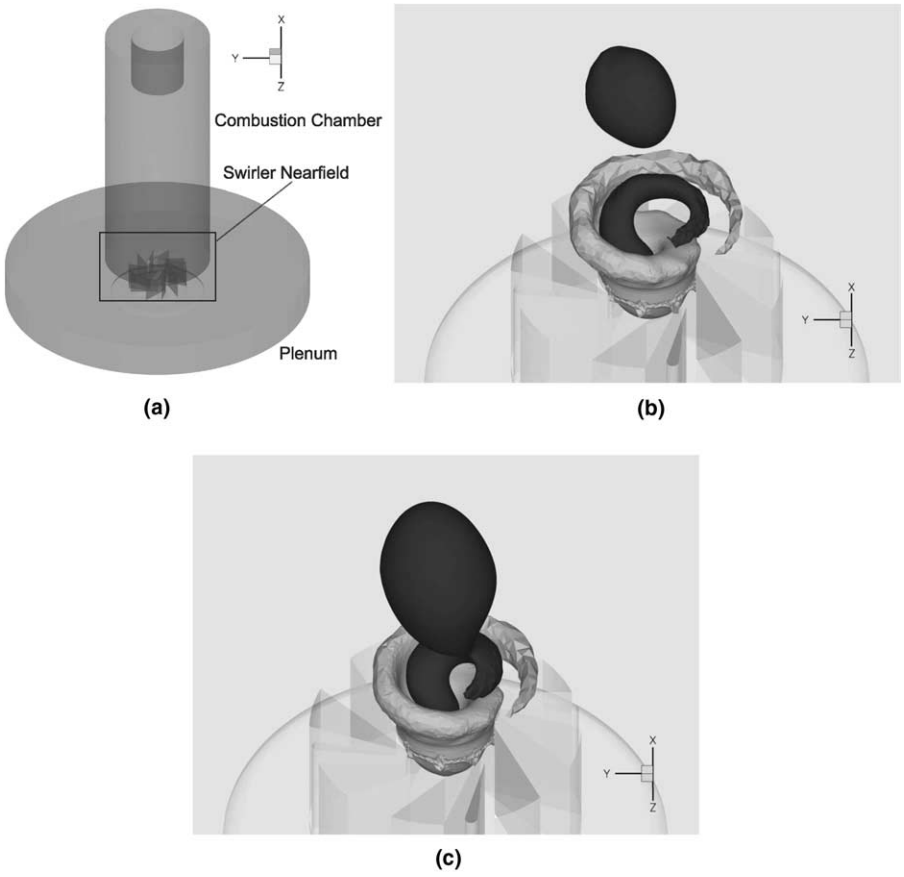

Fig. 8. Iso-surfaces of the axial velocity $u = -14$ m/s (dark) and 35 m/s (bright). (a) Cut-out for the figures (b) and (c), (b) SSG model and (c) k–ϵ model.

investigation, the evolution of the vortex breakdown was studied in detail (Section 6).

In order to evaluate the sensitivity to discretization errors, the calculation was carried out additionally on a refined computational grid with 3.3×10^6 elements (which corresponds to an increase in the number of elements of 30%) and with the second-order-backward-Euler scheme for temporal discretization. The results were identical to that on the coarser grid. Thus, we are confident that the influence of the discretization error is negligible.

4. Results

4.1. Predictions with the Reynolds stress model (SSG)

The Reynolds stress model used for closure of the Reynolds-averaged Navier–Stokes equations was that of Speziale et al. (1991) with a nonlinear pressure–strain model. After a short transition time, typical periodic structures evolved in the flow. An excerpt of the time series of the axial velocity at the two monitor points (Fig. 4) is shown in Fig. 5. Both time evolutions are strongly dominated by periodic patterns. In Figs. 6 and 7 a complete period of the quasi-periodic flow structures is shown by six instantaneous contour plots of the axial (x direction) velocity component in an azimuthal plane 5 mm downstream the swirler exit (Fig. 6) and in the meridional plane (x–y plane) (Fig. 7). As Fig. 6 reveals, the region of recirculating flow ($u < 0$) as well as the flow being discharged from the swirler ($u > 0$) are out of the center and do precess around the axis of symmetry. From Fig. 7 it is evident that first signs of symmetry breaking appear upstream of the divergent part of the swirler, and that the central recirculation zone penetrates upstream back into the swirler. As the axial velocity is the dominating component of the velocity vector, similar structures can be obtained by plotting the absolute value of the velocity.

For a better perception of the flow structures presented in Fig. 8(b) and (c), the orientation and view on the configuration used for these pictures is shown in Fig. 8(a). The three-dimensional structure of the predicted flow is visualized in Fig. 8(b) where two iso-surfaces of the axial velocity are plotted. The iso-surface of the fluid emerging from the swirler (axial velocity $u = 35$ m/s) is brightly colored. The iso-surface for $u = -14$ m/s is marked by the darker color and exhibits two separate regions of reversed flow. One which is nearly axisymmetric and resembles a bubble. It is located in the combustion chamber. The other one has a spiral shape and extends from the combustion chamber to the swirler nozzle. The spiral structure of the emerging fluid in Fig. 8 has an opposite sense of winding to the basic flow rotation which is in agreement with the experimental

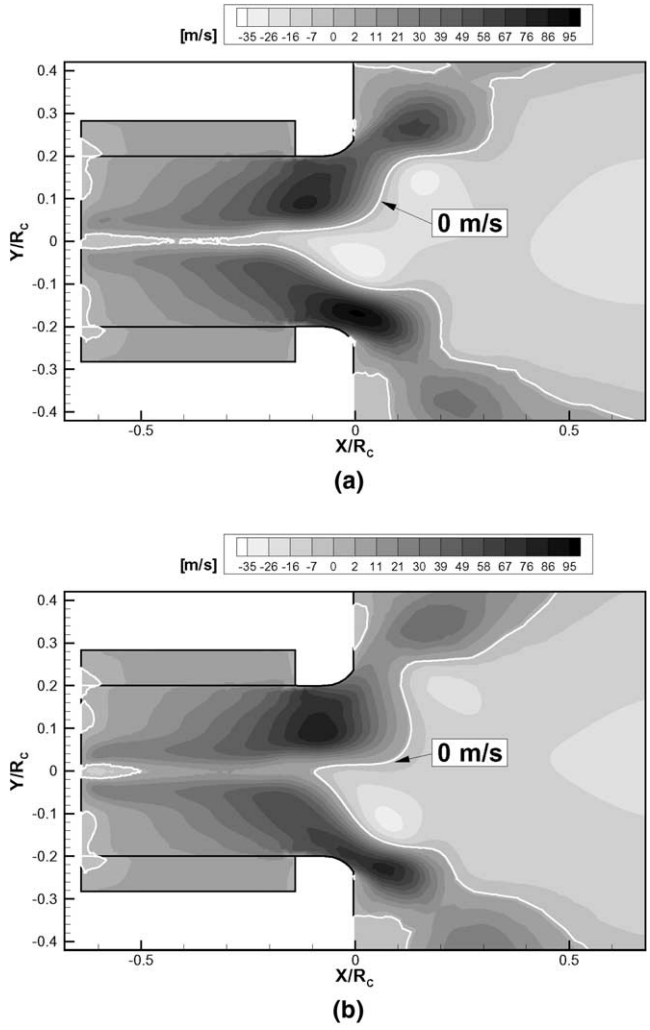

Fig. 9. Contour plots of the axial velocity and the contour line $u = 0$ m/s as predicted by the k–ϵ model. (a) Maximal penetration of reversed flow and (b) minimal penetration of reversed flow.

observations of Lambourne and Bryer (1961), Escudier and Zehnder (1982) and Brücker (1993).

As the temporal evolution (Figs. 6 and 7) indicates, there is a spiraling motion of the emerging fluid as well as of the recirculating fluid. These coupled flow zones gyrate with a frequency of about 1800 Hz. This is one of the dominating periodicities found in the time series at the monitoring point 2 (Fig. 5) which will be discussed in detail in a later section (see also Fig. 12).

4.2. Predictions with the two-equation model (k–ϵ)

The flow features described in the previous section could be completely reproduced by the k–ϵ turbulence model with the standard set of constants (Launder and Sharma, 1974). The differences to the results of the SSG model were small, which is confirmed by comparing Fig. 8(b) and (c). Consequently, plots equivalent to Figs. 6 and 7 are not presented for the k–ϵ prediction. Instead, the results as obtained by the k–ϵ turbulence model are used to discuss another flow feature. In Fig. 9 the contour plot of the axial velocity including the contour line of $u = 0$ m/s is presented for two instantaneous time steps. Close to the symmetry axis where the radial and the tangential velocity component are nearly vanishing, the zero velocity contour line indicates the stagnation point. The results as displayed in Fig. 9(a) reveal that there is a very thin zone of flow recirculating from the combustion chamber to the rear wall of the swirler. At a later time, the stagnation point is shifted downstream. It is now located at the onset of the divergent exit section of the swirler as shown in Fig. 9(b). Our results indicate a fairly periodic upstream and downstream movement of the stagnation point with a frequency of approximately 400 Hz which is different from the frequency of the vortex precession shown in Figs. 6 and 7. This oscillation of

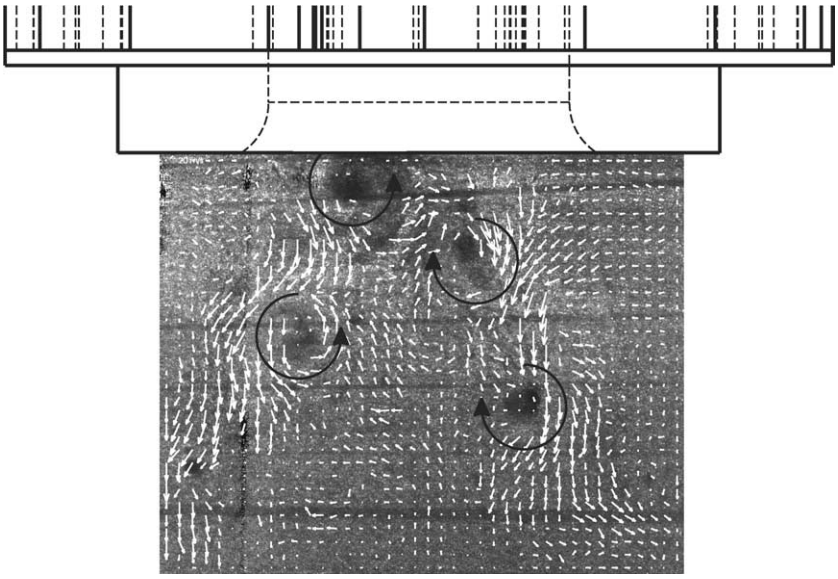

Fig. 10. Instantaneous PIV result of the flow structures in the meridional plane.

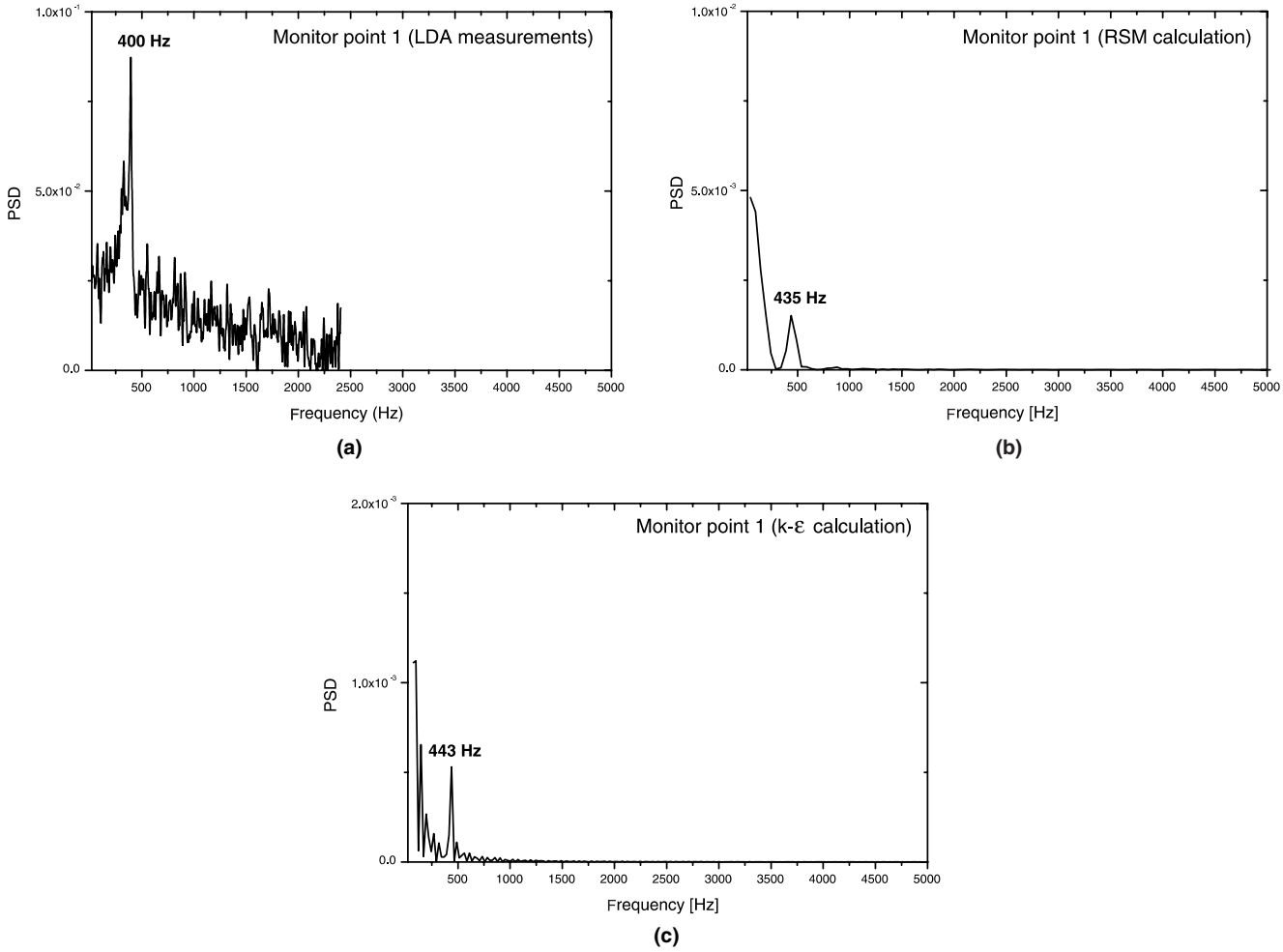

Fig. 11. Spectral power densities at monitor point 1. (a) FFT from LDA, (b) FFT from SSG model and (c) FFT from k–ϵ model.

the stagnation point is a common feature of vortex breakdown flows as Faler and Leibovich (1977) and Leibovich (1978) have observed for both modes of breakdown. Calculations with the Reynolds stress model showed similar results.

It was not expected to find such a similarity of the prediction with the different closure models, especially because it is known from many investigations, that the k–ϵ model leads in many cases to quite different results when predicting swirl flows compared to a full Reynolds stress transport approach (cf. Bradshaw, 1973; Speziale, 1991; Launder, 1996). Indeed, typical values for the Reynolds stress tensor in the nearfield of the swirler are predicted by the k–ϵ model six to seven times higher than those of the SSG model. Similarly, the turbulent eddy viscosity calculated from $\mu_t = \varrho C_\mu \frac{k^2}{\varepsilon}$ is three to four times higher for the k–ϵ prediction compared to the SSG model. A comparison of the typical ratio of the eddy viscosity μ_t to the molecular viscosity μ_l shows that $\frac{\mu_t}{\mu_l} \approx 500$ for the k–ϵ case and $\frac{\mu_t}{\mu_l} \approx 150$ for the SSG prediction. Therefore, it is quite clear that the Reynolds stresses are dominating the stress tensor in both cases, which might have been expected. From these findings it may be concluded that the complete stress tensor including laminar and turbulent effects may play an inferior role compared to the inertial and temporal terms in the Navier–Stokes equations for the flow case under consideration. It has to be kept in mind, that early theoretical considerations of Squire (1960) and Benjamin (1962) have treated the axialsymmetric vortex breakdown as an inviscid phenomenon and it was confirmed by recent numerical studies (cf. Brown and Lopez, 1990; Althaus et al., 1995; Wang and Rusak, 1997) that the mechanisms leading to the bubble type vortex breakdown are as a matter of fact mainly inviscid. In the light of these previous investigations, our findings which suggest an essentially inviscid mechanism for the turbulent, spiral type vortex breakdown might not be surprising.

5. Comparison to experimental results

5.1. Temporal fluctuations

In order to validate the numerical results, a test rig in 1:1 scale and with access for optical diagnostics to the combustion chamber was setup. 2D-LDA (Laser–Doppler anemometry) measurements (in backscatter mode) and

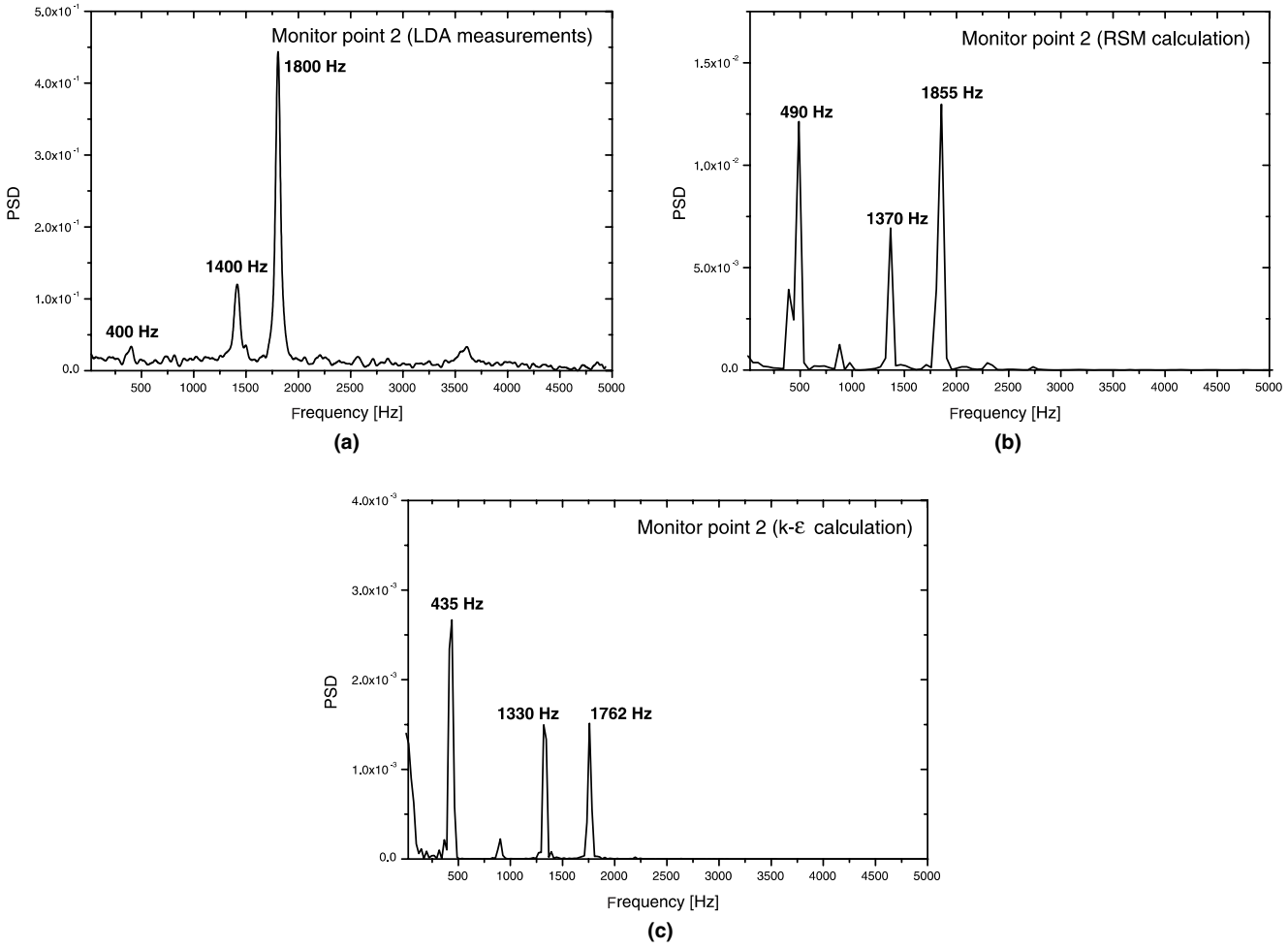

Fig. 12. Spectral power densities at monitor point 2. (a) FFT from LDA, (b) FFT from SSG model and (c) FFT from k–ϵ model.

Table 2
The Strouhal numbers corresponding to the frequency peaks of Figs. 11 and 12

	Sr_1 ($f \approx 1800$ Hz)	Sr_2 ($f \approx 1400$ Hz)	Sr_3 ($f \approx 400$ Hz)
LDA measurements	0.66	0.51	0.15
Results with k–ϵ model	0.65	0.49	0.16
Results with SSG model	0.68	0.50	0.16

PIV (particle image velocimetry) investigations have been performed at the same flow conditions as those investigated in the numerical computations (air flow at ambient pressure and temperature). Droplets generated by a Laskin-nozzle (90 vol% of the droplets smaller than 1.8 μm and 50 vol% smaller than 1.0 μm) were introduced in the plenum upstream of the swirler (which ensured a homogeneous distribution at the swirler inlet) and served as tracer particles. In Fig. 10, the instantaneous velocity field as recorded by PIV at a meridional cross-section of the combustion chamber is presented together with the schematic of the swirler exit. The two velocity components in the x–y plane are shown as vectors. Because of the strong centrifugal forces, the marker particles are

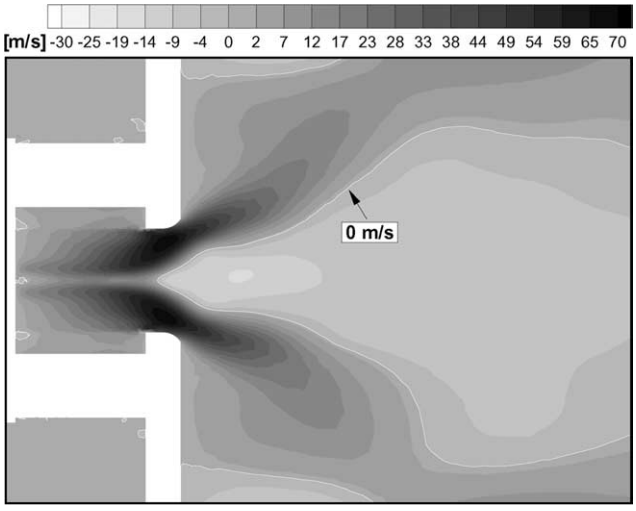

Fig. 13. Contour plot of the time-averaged axial velocity in the meridional plane.

moving radially outwards of the vortex core. The darker regions in Fig. 10 indicate that no velocity could be determined because of the absence of particles. Thus, these regions correspond to regimes of the vortex core. In

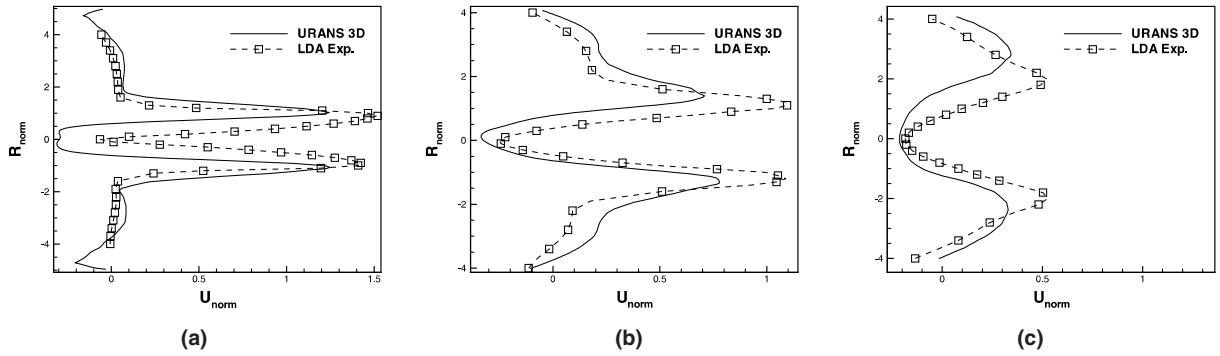

Fig. 14. Comparison of the radial time-averaged axial velocity profiles (normalized with $\bar{u}$) in various distances from the swirler exit. (a) $X/r_i = 0.5$, (b) $X/r_i = 1.5$ and (c) $X/r_i = 3.0$.

accordance with the numerical predictions, the experimental results show a helical structure. The circles in Fig. 10 indicate the sense of rotation of the spiraling vortex core. Moreover, the experiments also confirm that the vortex structure exhibits an axial displacement as it was found in the predictions (Fig. 7).

A more quantitative comparison is shown in Figs. 11 and 12. The power density spectra of the axial velocity component as obtained from a fast-Fourier-transform (FFT) of the LDA data are compared to those extracted from the calculations with the Reynolds stress model and the k–ϵ model. The power density spectra have been determined for monitor point 1 (Fig. 11) and monitor point 2 (Fig. 12). At monitor point 1, a predominant peak at around 400 Hz is found from the experiments as well as from the predictions. The peak of the calculated time series is at 440 Hz, about 10% higher than for the measured time series. For monitoring point 2, the spectra show three distinct peaks. One at 400 Hz which is also found at monitor point one and two additional ones at about 1400 Hz and 1800 Hz. Comparison to the experimental data reveals that the higher frequencies were predicted with a deviation of less than 3%.

The discrepancy between the amplitudes of the power density peaks of the measured and the numerical time series in Figs. 11 and 12 can be partially attributed to the time series duration. While the measurements provided time series of at least 10 s length, the numerical time series were limited to 0.02 s (starting and settling period not included) in order to limit the computational effort. Additionally, within the URANS approach the main part of the turbulent spectrum is modelled and, therefore, this fraction is not included in the spectra. Therefore, exactly matching the amplitudes of the experiment by the predictions cannot be expected. Nevertheless, as the frequencies are predicted correctly also the Strouhal numbers as defined in Table 1 are in very good agreement (Table 2).

5.2. Time averaged flowfield

For deriving the time averaged flow quantities, the calculated flowfield was averaged over 2500 time steps, which corresponds to a physical time period of 0.025 s. This time period contains circa 10 pulsation cycles of the stagnation point ($f \approx 400$ Hz) and more than 45 precession cycles ($f \approx 1800$ Hz). In Fig. 13 the averaged axial velocity in the meridional plane is presented. The spiral structure inside the swirler and the combustion chamber is completely removed by the averaging process, and the averaged flow quantity exhibits a high degree of axisymmetry, especially in the regions where the flow is dominated by high periodic fluctuations, namely the exit of the swirler and the inlet of the combustion chamber. From the time averaged velocity field as presented in Fig. 13, radial velocity profiles were extracted at three different distances downstream the swirler exit. These axial velocity profiles are compared with the time averaged LDA measurements (for which the integration period is at least 10 s) in Fig. 14. Although the radial distributions of the measured and the calculated profiles have similar characteristics, there is still a deviation of 15–30%. One source of uncertainty is the separation of the tracer particles in the LDA measurements caused by high centrifugal forces which was also observed in the PIV snapshot in Fig. 10. Consequently the velocities of the vortex core region (with a tracer particle deficit) are underestimated compared to the regions at the edge of the vortex core (with a tracer particle excess) by the averaging process. As Hehle et al. (2002) have shown, in such situations a phase-resolved averaging gives different and potentially better estimations of the velocity than simple averaging over all recorded events. A further advantage of this averaging technique was shown in the work of Cala et al. (2004), where phase averaging was combined with the LDA technique. For a similar flow case Cala et al. (2004) were able to extract the spiraling vortex core as well as the helical recirculation zone from the phase-averaged data, which is impossible by means of conventional time averaging.

6. Breakdown-mode selection

A further question to be studied was how the vortex breakdown mode selection takes place. It was one of the crucial questions of present research, if and how the spiral

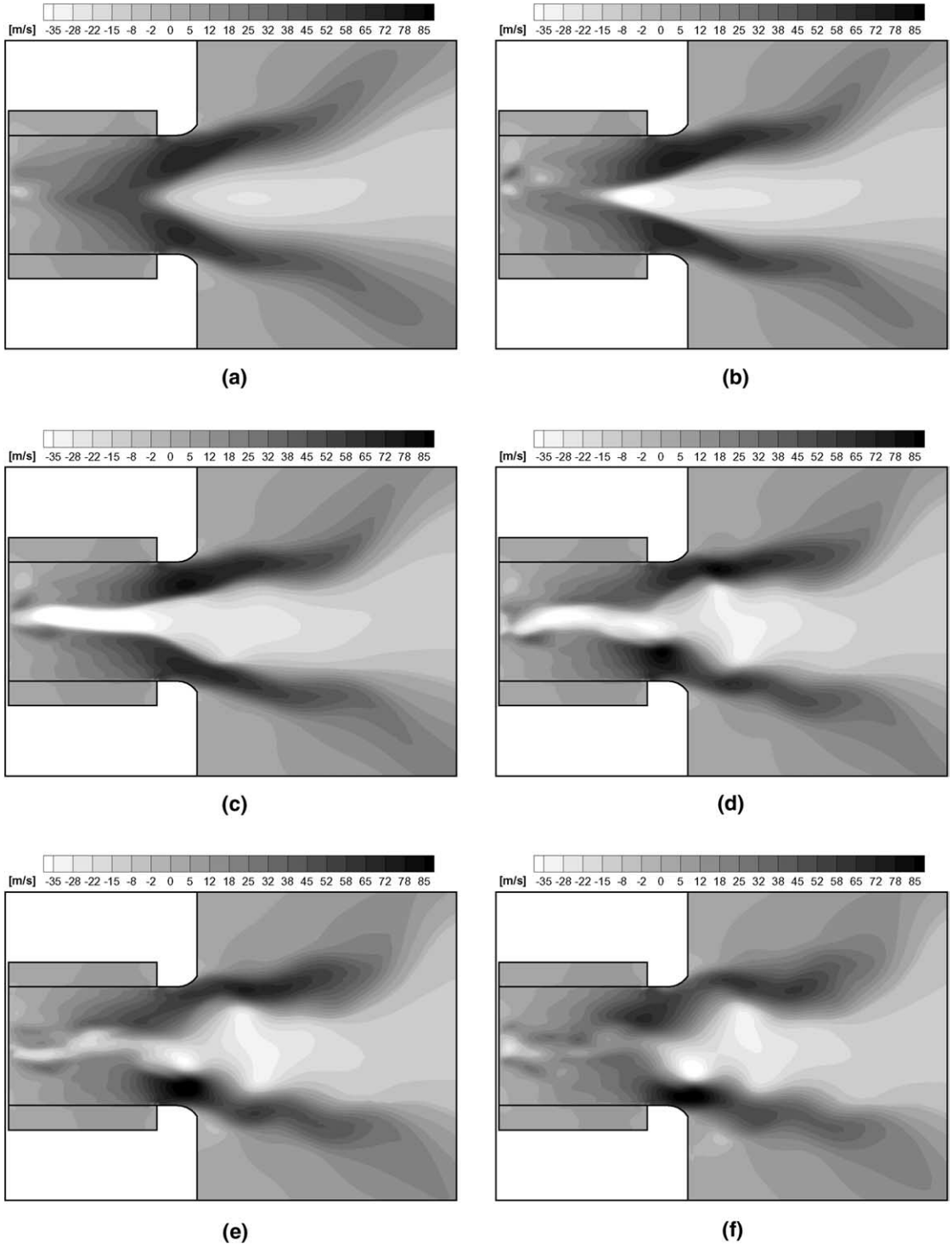

Fig. 15. The transition from the bubble type vortex breakdown to the spiral type unsteady vortex breakdown in the meridional plane (SSG model). (a) $\Delta T = 1 \times 10^{-4}$ s, (b) $\Delta T = 3 \times 10^{-4}$ s, (c) $\Delta T = 5 \times 10^{-4}$ s, (d) $\Delta T = 7 \times 10^{-4}$ s, (e) $\Delta T = 8 \times 10^{-4}$ s and (f) $\Delta T = 9 \times 10^{-4}$ s.

type and the bubble type vortex breakdown are related to each other (Leibovich, 1978, 1984; Escudier, 1988; Lucca-Negro and O'Doherty, 2001). Although the idea that the bubble type is the basic breakdown type and the transition to spiral type evolves from a helical instability in the bubble type vortex breakdown wake (Escudier et al., 1982) or in the shear layers enclosing the recirculation bubble (Escudier and Keller, 1983) was proposed 20 years ago, there was no prove of this theory until the experimental work of Brücker and Althaus (1995). In their setup the spiral type mode evolved from the bubble type, which always was observed first. The next important breakthrough were

direct numerical simulations (DNS) of Ruith et al. (2003). They found that helical instabilities with an azimuthal mode of $m = -1$ (spiral structure) and $m = -2$ (double helix) evolved in the wake of the primary bubble type vortex breakdown. However, the work of Brücker and Althaus (1995) as well as the calculations of Ruith et al. (2003) were limited to low Reynolds number ($Re \approx 100$–300) flows which were unaffected by the containment.

In order to investigate if the scenario is also valid for the highly turbulent flow under concern, first a steady calculation was performed until the state was reached where the global mass and momentum balances are satisfied with an error of 1–2%. Starting out from these results the unsteady calculations were commenced. The SSG turbulence model was used for closure of the Reynolds stress transport equations. In Fig. 15 the transition sequence from a quasi-axisymmetrical vortex breakdown in the combustion chamber to the spiral structures dominating the swirler exit is depicted. At the beginning of the time dependent calculation, the reference time was set to zero. The snapshot in Fig. 15(a) shows the axial velocity distribution in the meridional plane for a time step 10^{-4} s after the unsteady calculation was started. It reveals a central, highly axisymmetric recirculation zone, which is typical for the bubble type vortex breakdown. At the next displayed time step ($\Delta T = 3 \times 10^{-4}$ s), the recirculation zone moves upstream and penetrates into the swirler. Simultaneously, the (axial) recirculation velocity increases up to -30 m/s and more. The following time step ($\Delta T = 5 \times 10^{-4}$ s) illustrates that the pronounced recirculation zone on the axis of the swirler extends to the backplane of the swirler. Now the vortex breakdown also dominates the central channel of the swirler, nonetheless the flow is still mainly axisymmetric. The first clear signs of an asymmetric flow are visible at the time step $\Delta T = 7 \times 10^{-4}$ s, where the emerging fluid shows an axial displacement of the velocity maxima, as well as a strong reverse flow on the central axis. This picture is more pronounced in the last two time steps presented in Fig. 15(e) and (f). Both snapshots elucidate that the recirculation velocity inside the swirler is decreasing and, at the same time, an axial velocity maximum develops in close vicinity to the minimum marking the deflected vortex core, which deviates significantly from the axis of symmetry. Fig. 15(f) clearly indicates the appearance of the spiral type vortex breakdown.

The physical time for the transition from the bubble type to the spiral type vortex breakdown adds up to about 10^{-3} s, which corresponds to approximately two rotations of the spiralling vortex core. The transition sequence presented in Fig. 15 is similar to that observed by Brücker and Althaus (1995) from particle tracking velocimetry (PTV) investigations. It provides a qualitative link to the DNS calculations of Ruith et al. (2003). Our results suggest that the mechanism which is responsible for the vortex breakdown mode selection at the high Reynolds number is similar to that reported by Ruith et al. (2003) for the laminar flow at Reynolds numbers of $Re \approx 100$–300.

7. Concluding remarks

A precessing (S-type) vortex breakdown with complex dynamical behavior was predicted with the URANS method. Two distinct quasi-periodic flow features were captured. First, the flow emerging from the nozzle as well as the recirculating flow exhibit a spiral shape and are gyrating around the axis of symmetry. It was found that this precession has a distinct frequency which could be observed in the time series of the axial velocity. Second, the axial pulsation of the vortex breakdown gives rise to a second distinct frequency. The helical structures of the spiraling vortex core as well as predominant frequencies were confirmed by PIV visualization and LDA measurements.

Although it is well known that the k–ϵ model suffers from drawbacks like over-prediction of eddy viscosity and is not capable to capture the anisotropic turbulence of swirling flows (cf. Bradshaw, 1973), the highly unsteady flow patterns of the present flow could be predicted with good accuracy. The two different turbulence models yielded quite different turbulent quantities. But the recovering of the unsteady flow structures was relatively insensitive to the exact values of the turbulent quantities predicted by the different turbulence models. Thus, it may be concluded that the essential mechanism leading to the spiral type vortex breakdown is even in the turbulent flow case not much affected by the turbulence of the flow.

Another frequently mentioned limitation of two-equation turbulence models is the so-called spectral gap, which means that an appropriate difference between the time scales of the main flow and the turbulent time scales is required. In the present case it was shown that, although the time scales are not separated, the URANS models performed quite well. Thus, there seems to be no inherent limitation for the resolution of transient flow phenomena up to several kHz. This finding was pointed out by Noll et al. (2001) previously. Additionally, it should be mentioned that the resolution of the unsteady flow features was very sensitive to the grid size in the region of the helical structures. Especially the k–ϵ model has the tendency to damp the development of the instability leading to the spiral shaped flow structures. Only if the cell size at the swirler exit was reduced to below 0.5×10^{-3} m, the flow features could be reproduced in detail. This confirms the statement of Menter et al. (2003) that there is no absolute scale introduced by the statistical averaging until the grid limit is reached.

The time averaged flowfields from the numerical calculations with the SSG Reynolds stress model have been found to be in reasonable agreement with experimental results. In the time averaged flowfield the spiral structures are removed by averaging over a relatively short time span.

From the investigation of the breakdown mode selection, it was found that the transition from bubble to the spiral type vortex breakdown is similar to the one in the laminar flows.

Finally, it is worth mentioning that combustion might change the flowfield characteristics seriously as stated

previously by Escudier and Keller (1985) and Escudier (1988). This effect has been confirmed by extensive experimental and numerical studies of Schildmacher et al. (2003) and Selle et al. (2004) revealing that the precessing vortex structure visible in the cold flow might disappear in reacting flow. This phenomenon is due to the axial flow acceleration caused by the flame. As Escudier and Keller (1985) have mentioned, by axial flow acceleration the flow can be turned from a subcritical state after vortex breakdown to a supercritical state.

Acknowledgment

This work was partially supported by AG TURBO, Teilverbundprojekt Kraftwerk und Kraftwerkssysteme, Projekt Nr. 4.4.4 A. Grant 0327091A, which is gratefully acknowledged.

References

Althaus, W., Brücker, C., Weimer, M., 1995. Breakdown of slender vortices. In: Green, S.I. (Ed.), Fluid Vortices. Kluwer Academic, Dordrecht, pp. 373–426.

Barth, T.J., Jespersen, D.C., 1989. The design and application of upwind schemes on unstructured meshes. AIAA Paper 89-0366, Reno, Nevada, AIAA 27th Aerospace Science Meeting and Exhibit.

Benjamin, T.B., 1962. Theory of the vortex breakdown phenomenon. Journal of Fluid Mechanics 14, 593–629.

Bradshaw, P., 1973. Effects of streamline curvature on turbulent flow. Tech. Rep. AGARDograph No.169, AGARD, London.

Brown, G.L., Lopez, J.M., 1990. Axisymmetric vortex breakdown. Part 2. Physical mechanisms. Journal of Fluid Mechanics 221, 553–576.

Brücker, C., 1993. Study of vortex breakdown by particle tracking velocimetry (PTV). Part 2. Spiral-type vortex breakdown. Experiments in Fluids 14, 133–139.

Brücker, C., Althaus, W., 1995. Study of vortex breakdown by particle tracking velocimetry (PTV). Part 3. Time-dependent structure and development of breakdown-modes. Experiments in Fluids 18, 174–186.

Cala, C.E., Fernandes, E.C., Heitor, M.V., Shtork, S.I., 2004. LDA analysis of PVC-central recirculation zone interaction in a model vortex burner. In: Adrian, R.J., Durão, D.F.G., Heitor, M.V., Hishida, K., Tropea, C. (Eds.), Proceedings of the 12th International Symposium on Applications of Laser Techniques to Fluid Mechanics. June 12–15, 2004, Lisbon, Portugal.

Durbin, P.A., 2002. A perspective on recent developments in RANS modeling. In: Rodi, W., Fueyo, N. (Eds.), Proceedings of Engineering Turbulence Modelling and Experiments, vol. 5. Elsevier Science Ltd., pp. 3–16.

Escudier, M.P., 1987. Confined vortices in flow machinery. Annual Review of Fluid Mechanics 19, 27–52.

Escudier, M.P., 1988. Vortex breakdown: observations and explanations. Progress in Aerospace Science 25, 189–229.

Escudier, M.P., Keller, J.J., 1983. Vortex breakdown: a two-stage transition. In: Aerodynamics of Vortical Type Flows in Three Dimensions. AGARD-CP-342, pp. 25-1–25-8.

Escudier, M.P., Keller, J.J., 1985. Recirculation in swirling flows: a manifestation of vortex breakdown. AIAA Journal 23, 111–116.

Escudier, M.P., Zehnder, N., 1982. Vortex-flow regimes. Journal of Fluid Mechanics 115, 105–121.

Escudier, M.P., Bornstein, J., Maxworthy, T., 1982. The dynamics of confined vortices. Proceedings of the Royal Society of London A 382, 335–360.

Faler, J.H., Leibovich, S., 1977. Disrupted states of vortex flow and vortex breakdown. Physics of Fluids 20, 1385–1400.

Guo, B., Langrish, T.A.G., Fletcher, D.F., 2001. Simulation of turbulent swirl flow in an axisymmetric sudden expansion. AIAA Journal 39, 96–102.

Gupta, A.K., Lilley, D.G., Syred, N., 1984. Swirl Flows. Abacus Press, Tunbridge Wells.

Hall, M.G., 1972. Vortex breakdown. Annual Review of Fluid Mechanics 4, 195–218.

Hehle, M., Schäfer, O., Koch, R., Wittig, S., 2002. Experimentelle Untersuchung von periodischen Instationaritäten an einem neuartigen Zerstäuber mittels phasenaufgelöster PDA-Messungen. In: 7. Workshop über Techniken der Fluidzerstäubung und Untersuchungen von Sprühvorgängen. No. A 870 Verfahrenstechnik. TU Bergakademie Freiberg, pp. 123–132.

Iaccarino, G., Ooi, A., Durbin, P.A., Behnia, M., 2003. Reynolds averaged simulations of unsteady separated flow. International Journal of Heat and Fluid Flow 24, 147–156.

Lambourne, N.C., Bryer, D.W., 1961. The bursting of leading-edge vortices—some observations and discussion of the phenomenon. No. 3282 in Reports and Memoranda. Aeronautical Research Council, pp. 1–36.

Launder, B.E., 1996. Advanced turbulence models for industrial applicationsERCOFTAC Series. Kluwer Academic Publishers, Dordrecht, pp. 193–231 (Chapter 5).

Launder, B.E., Sharma, B.I., 1974. Application of the energy-dissipation model of turbulence to the calculation of flow near a spinning disc. Letters in Heat and Mass Transfer 1, 131–138.

Leibovich, S., 1978. The structure of vortex breakdown. Annual Review of Fluid Mechanics 10, 221–246.

Leibovich, S., 1984. Vortex stability and breakdown: survey and extension. AIAA Journal 24, 1192–1206.

Lucca-Negro, O., O'Doherty, T., 2001. Vortex breakdown: a review. Progress in Energy and Combustion Science 27, 431–481.

Menter, F.R., Kuntz, M., Bender, R., 2003. A scale-adaptive simulation model for turbulent flow predictions. AIAA Paper 2003-0767, Reno, Nevada, AIAA 41st Aerospace Science Meeting and Exhibit.

Noll, B., Schütz, H., Aigner, M., 2001. Numerical simulation of high-frequency flow instabilities near an airblast atomizer. ASME Paper 2001-GT-0041, New Orleans, Louisiana.

Ruith, M.R., Chen, P., Meiburg, E., Maxworthy, T., 2003. Three-dimensional vortex breakdown in swirling jets and wakes: direct numerical simulation. Journal of Fluid Mechanics 486, 331–378.

Sarpkaya, T., 1971. On stationary and travelling vortex breakdowns. Journal of Fluid Mechanics 45, 545–559.

Schildmacher, K.-U., Koch, R., Krebs, W., Prade, B., 2003. Experimental investigation of the interaction of flame front fluctuations with combustion of a premixing gas turbine burner. In: 21. Deutscher Flammentag, pp. 297–302.

Selle, L., Lartique, G., Poinsot, T., Koch, R., Schildmacher, K.-U., Krebs, W., Kaufmann, P., Veynante, D., 2004. Compressible large eddy simulation of turbulent combustion in complex geometry on unstructured meshes. Combustion and Flame 137, 489–505.

Speziale, C.G., 1991. Analytical methods for the development of Reynolds-stress closures in turbulence. Annual Review of Fluid Mechanics 23, 107–157.

Speziale, C.G., Sarkar, S., Gatski, T.B., 1991. Modeling the pressure–strain correlation of turbulence: an invariant dynamical systems approach. Journal of Fluid Mechanics 227, 245–272.

Squire, H.B., 1960. Analyses of the 'vortex breakdown' phenomenon, Part 1. Aeronautics Department, Imperial College, London, Report No. 102.

Wang, S., Rusak, Z., 1997. The dynamics of a swirling flow in a pipe and transition to axisymmetric vortex breakdown. Journal of Fluid Mechanics 340, 177–223.

Wegner, B., Maltsev, A., Schneider, C., Sadiki, A., Dreizler, A., Janicka, J., 2004. Assesment of unsteady RANS in predicting swirl flow instability based on LES and experiments. International Journal of Heat and Fluid Flow 25, 528–536.